Properties of Lean Turbulent Methane-Air Flames With Significant Hydrogen Addition

Marc S. Day, Xinfeng Gao, John B. Bell

Lawrence Berkeley National Laboratory, Berkeley, CA 94720, USA

Abstract

We examine the combustion of mixed H_2-CH_4-air fuels using two-dimensional simulations that incorporate detailed kinetics and a mixture-averaged model for differential species transport. The mixtures range from lean H_2-air at ϕ=0.37 to lean CH_4-air at ϕ=0.7. For each mixture, we compute the quasi-steady propagation of a flame into flow with superimposed low-level turbulent fluctuations. We examine the resulting global flame characteristics, and quantify how the chemistry depends on local flame curvature. We then examine in more detail how the methane chemistry is modulated by the presence of hydrogen. In particular, we find that the local methane burning speed shows a strong positive correlation with local flame curvature when sufficient hydrogen is added to the mixture. Moreover, for higher hydrogen concentrations, the mixtures exhibit cellular burning patterns that are traditionally associated with thermodiffusively unstable fuel mixtures. Various pathways for the oxidation of methane are identified and are shown to be amplified considerably in the presence of H_2 combustion, which varies considerably along the flame surface.

Keywords: premixed lean combustion, turbulent combustion, hydrogen-methane mixtures

---

1. Introduction

There has been considerable recent interest in the development of fuel-flexible lean premixed systems for stationary power generation. Compared to non-premixed, or stoichiometric premixed systems, devices that burn lean premixed fuels have the potential to reduce emissions because they operate at reduced the exhaust gas temperature, and thus generate considerably less thermal NO_x. However, mixtures that are lean enough to achieve sub-ppm NO_x emissions levels become extremely difficult to stabilize against global extinction due to lean blow-off. One approach to stabilizing against these events entails the addition of small amounts of hydrogen to the premixed fuel stream. Experimental studies of Littlejohn and Cheng [1] and Cheng et al. [2] demonstrate the feasibility of this strategy for a range of fuels in atmospheric and elevated pressure environments, in terms of improved extinction limits and emissions reduction. The behavior of H_2-CH_4 mixtures has also been investigated experimentally by Wicksall et al. [3], Lawn and Schefer [4], Coh$\acute{e}$ et al. [5], Halter et al. [6], Mandilas et al. [7], Strakey et al. [8], Kim et al. [9] and Fairwether et al. [10].

Premixed combustion of H_2-CH_4 mixtures has also been studied computationally. Jackson et al. [11] investigated how H_2 addition influences lean-premixed CH_4 flame response to high strained flows and their results indicate that increasing H_2 in the fuel significantly increases flame speeds and thus extinction strain rates. Hawkes and Chen [12] used DNS to compare a lean methane flame near the extinction limit with a hydrogen enriched flame. They found that the addition of methane improved flame stability and reduced CO emissions, but also increased the emission of NO. Sankaran and Im [13] looked at stretch effects on flammability and Markstein number for hydrogen/methane mixtures. Dunstan and Jenkins [14] examined the effect of hydrogen addition to methane flame kernels. Vreman et al. [15] investigated lean premixed turbulent Bunsen hydrogen-methane flames, finding enhanced/reduced local burning velocities in regions convex/concave toward the reactants, respectively. In addition, de Goey et al. [16] present a theoretical analysis of the structure of CH_4-H_2-air flames.

The focus of much of the previous work has been on the addition of a small amount of H_2 to improve the stability of hydrocarbon flames near the flammability limit. In the present work, we focus instead on fuel mixtures with a much higher hydrogen content. These mixtures provide a reasonable surrogate for a range of refinery gases and other fuels that might arise from coal or biomass gasification processes. It is well-known that lean H_2-air mixtures themselves burn in cellular flame structures due to the thermodiffusive instability. A feature of the cellular burning structures is that they generate significant nonuniformity along the flame surface, where temperatures can far exceed the adiabatic flame temperature of the mean mixture. See for exmaple [17, 18] and references cited therein. This will likely have dramatic impact on the global flame stability and emissions generations in practical devices. It is reasonable then to expect that there will be an enrichment level beyond which the hydrocarbon fuel will begin to exhibit cellular burning patterns as well. Cheng et al. [2] considered a range of H_2/CH_4 mixtures in a low-swirl experimental burner. They found that for up to 60% hydrogen the large-scale flow patterns and flame stabilization mechanism remained essentially similar to that of the pure CH_4-air flames; however, with higher levels of hydrogen they observed significant changes in flame structure. In particular, for hydrogen content of 80% or more in the fuel, the flame attached to the burner nozzle, which represents a shift in the global stabilization mechanism.

Here, we examine the combustion of mixed H_2-CH_4 fuels using detailed 2D simulations. We consider a broad range of H_2 enrichment of a lean (ϕ=0.7) CH_4-air mixture. For each mixture, we compute the quasi-steady propagation of a flame into flow with superimposed low-level turbulent fluctuations. We examine the global flame characteristics, and quantify how the local fuel consumption depends on flame curvature. We then examine in more detail how the methane chemistry is modulated by the presence of hydrogen.

2. Computational Framework

The simulations reported here are performed with the adaptive low Mach number algorithm presented in Day and Bell [19]. The model includes a mixture-averaged formulation for differential species diffusion, and heat and momentum transport. With these assumptions, the system of low Mach number flow equations for an open domain is

$$\frac{\partial \rho U}{\partial t} + \nabla \cdot \rho U U = -\nabla \pi + \nabla \cdot \tau, \tag{1}$$

$$\frac{\partial \rho Y_m}{\partial t} + \nabla \cdot U \rho Y_m = \nabla \cdot \rho D_m \nabla Y_m + W_m \dot{\omega}_m, \tag{2}$$

$$\frac{\partial \rho h}{\partial t} + \nabla \cdot U \rho h = \nabla \cdot \frac{\lambda}{c_p} \nabla h + \sum_m \nabla \cdot h_m \Big(\rho D_m - \frac{\lambda}{c_p} \Big) \nabla Y_m, \tag{3}$$

where ρ is the gas mixture density, U is the gas mixture velocity, τ is the stress tensor, and π is the perturbational pressure field ($\pi/p_0 \sim \mathcal{O}(M^2)$, where M is the Mach number. Y_m is the mass fraction of species m, $\dot{\omega}_m$ is the net molar production rate for species m due to chemical reactions, W_m is the molecular weight of species m, h is the mass-weighted enthalpy of the gas mixture, and λ is the thermal conductivity. In addition, c_p is the specific heat of the mixture, and $h_m(T)$ and D_m are the enthalpy and mixture-averaged diffusion coefficients of species m, respectively. These equations are supplemented by the ideal gas law for a perfect gas mixture. Transport coefficients, thermodynamic data and chemical rate expressions are specified by the DRM19 reduced methane combustion mechanism [20], and consists of 21 species and 84 fundamental Arrhenius reactions.

The basic numerical discretization combines a symmetric operator-split treatment of chemistry and transport with a density-weighted approximate projection method. The projection method is used to impose a constraint on the velocity divergence such that a conservative integration of the species mass and total enthalpy simultaneously satisfies the equation of state. Time integration of the algorithm proceeds on the scale of advective transport. Faster diffusion and chemistry processes are treated time-implicitly. This integration scheme is embedded in an adaptive mesh refinement algorithm framework based on a hierarchical system of rectangular grid patches. The solution hierarchy is advanced in time with subcycling using a time stepsize appropriate to the CFL constraint at each level. The refinement levels are coupled together in a way that satisfies discrete conservation of mass and enthalpy and the elliptic divergence constraint. The overall algorithm is second-order accurate in both space and time.

The flow configuration initializes a flat flame propagating downward in a square domain, 8cm × 8cm. A cold fuel-air mixture enters the domain through bottom boundary, and hot combustion products exit the domain through the top. The remaining computational boundaries are periodic. Along the inflow face we use a feedback control algorithm [21] to dynamically adjust the mean gas inflow velocity so that the mean flame location remains stationary within the domain. Here, we set the mean flame location to 3 cm above the inflow face. Turbulent fluctuations are introduced into the inlet flow by superimposing a precomputed zero-mean fluctuating velocity field onto the time-dependent boundary inflow. The fluctuations are generated by an auxiliary calculation, initialized using a random velocity field with a prescribed energy spectrum [22]:

$$E(k) = \frac{(\frac{k}{k_i})^4}{[1+(\frac{k}{k_i})^2]^{\frac{17}{6}}} e^{-\frac{9}{4}(\frac{k}{k_d})^{\frac{4}{3}}} \qquad (4)$$

where k is the wavenumber, $k_d = 6400$ cm^{-1} and $k_i = 65$ cm^{-1}. This random field was evolved using an incompressible flow solver to adjust the phasing of the velocity fields. The resulting synthetic turbulence is isotropic with an integral scale $\ell_t = 3.0$ mm, with an intensity, $u' = 18.5$ cm/s.

We consider six different H_2/CH_4/air mixtures, defined in Table 1. For later reference, the table also includes the laminar burning speed, s_{lam}, temperature at the location of peak fuel consumption, T_{peak} and the thermal thickness, δ_{lam}, of the 1D steady flames with the corresponding fuel mixture. These six cases are evolved numerically using a base grid of 256×512 cells with 3 additional levels of refinement, each by a factor of 2. The finest grids, which dynamically track the flame, have uniform cell size, $\Delta x = 39.6\mu$m. Refined grids also track vortical features of the flow. A statistically stationary solution is obtained prior collecting data for diagnostics.

3. Results and Discussions

Figure 1 shows typical snapshots of flames A-F, taken after each have reached quasi-steady solutions. The main images depict the temperature field; the mean flow is upward, the flames burn down. Insets in each figure show the narrow band of fuel consumption at the flame surface over the small box indicated. Note that Cases A-E show the consumption rate of H_2, while Case F shows the consumption of CH_4 (there is no H_2 in the fuel). In Case E, there is a narrow layer of H_2 production parallel to the destruction layer. The various mixtures exhibit a range of salient characteristics. In Case F, for example, the fuel consumption layer is remarkably uniform even though the flame shape is quite kinked in regions. The overall shape of the flame is dominated by features characteristic of the hydrodynamic instability [23] interacting with weak turbulence, showing long bulbous sections of flame with positive curvature that are separated by short sections with high negative curvature. While similar behavior is evident in the five other cases, the addition of hydrogen coincides with the additional appearance of finer-scale scalloped cellular burning structures characteristic of the thermodiffusive instability. As these flames evolve in a quasi-steady fashion, the cell structures develop spontaneously along the flame surface in regions of low curvature: local fuel consumption drops quickly, and the reactive layer recedes downstream. On either side of this extinction zone, pairs of strongly burning flame arcs simultaneously develop that then seem to persist indefinitely, annihilated only when large-scale flame folding events lead to extinguished pockets of fuel that propagate into the products.

In order to quantify the variability in the burning along the surface, we construct a local measure of the flame propagation speed and examine its relationship to flame surface curvature. Following the procedure outlined in [21] we construct normals that are positioned along the isotherm, $T = T_{peak}$ and that extend into both the reactants and products well beyond where the fuel consumption levels drop to noise levels. Spanning the space between these normals, we define integration volumes, Ω_k, that collectively tile the entire region where fuel is consumed. A local burning speed for species m may then be defined on Ω_k

$$S^{loc,k}_{c,m} = \frac{-1}{(\rho Y_m)_{in} L} \int \dot{\omega}_m W_m \, d\Omega_k$$

L is the length of flame contour contained in the volume, and $(\rho Y_m)_{in}$ is the upstream fuel mass density. For our mixed fuels, this construction defines two burning speeds, S^{loc}_{c,H_2} and $S^{loc}_{c,\mathrm{CH}_4}$. Note that when both fuels are fully consumed at the flame surface, the integral of each of the two diagnostics should lead to the same global flame propagation speed.

Figure 2 shows S^{loc}_{c,H_2} and $S^{loc}_{c,\mathrm{CH}_4}$ vs. local curvature of the flame (scaled to the corresponding flame thickness, given in Table 1). Here, we follow the convention that positively curved regions have center of curvature in the products. The pure methane case shows remarkably constant burning speeds across the entire range of curvature. For Cases B and C, even though S^{loc}_{c,H_2} shows higher sensitivity to flame curvature than $S^{loc}_{c,\mathrm{CH}_4}$, a significant Markstein effect is generated for the CH_4 consumption. Indeed Cases B and C even show regions of methane flame extinction or significantly reduced methane burning speeds. It is also interesting to note that with increasing H_2 concentration, the mean H_2 burning speed in the flat regions of the flame (zero curvature) is increasingly higher than the corresponding value of s_{lam}. These observations suggest that a simple constant flame-speed model or even a model that includes a simple curvature correction based on classical Markstein theory would be unable to properly account for the range of conditions encountered in mixed fuels containing significant amounts of hydrogen.

We next examine the effect of H_2 fuel on methane combustion for the mixed fuel cases. There are four major reactions that play a significant role in the oxidation of methane:

$$\mathrm{O} + \mathrm{CH}_4 \rightleftharpoons \mathrm{CH}_3 + \mathrm{OH} \qquad (\mathbf{R_7})$$

$$\mathrm{H} + \mathrm{CH}_4 \rightleftharpoons \mathrm{CH}_3 + \mathrm{H}_2 \qquad (\mathbf{R_{32}})$$

$$\mathrm{OH} + \mathrm{CH}_4 \rightleftharpoons \mathrm{CH}_3 + \mathrm{H}_2\mathrm{O} \qquad (\mathbf{R_{49}})$$

$$\mathrm{H} + \mathrm{CH}_3(+\mathrm{M}) \rightleftharpoons \mathrm{CH}_4(+\mathrm{M}) \qquad (\mathbf{R_{31}})$$

Reactions, $\mathbf{R}_7$, $\mathbf{R}_{32}$, and $\mathbf{R}_{49}$ consume CH_4; $\mathbf{R}_{31}$ is a recombination reaction that generates CH_4 in the flame zone. As the overall reaction process increases in intensity, each of these contributing reactions becomes stronger. Figure 3 illustrates the amplification of these four reactions individually from steady flat flame profiles, and shows a strong correlation with the local H_2 consumption rate. Case B, which is almost entirely premixed hydrogen shows amplifications of these rates of up to four times for the reactions involving the H atom–both consuming and producing CH_4, and up to 2.5 for the other two reactions otherwise. Cases D and E are less sensitive to the local hydrogen consumption; thus, we see that for increasing levels of H_2, the sensitivity of this amplification increases, but it saturates beyond Case C.

We also observe a shift in relative strength between these reactions as a function of the local hydrogen consumption speed, S^{loc}_{c,H_2}. In Figure 4, we plot the consumption due to each reaction integrated over each Ω_k normalized the total net methane consumption over Ω_k, and plotted versus the local value of S^{loc}_{c,H_2}. As the burning of H_2 becomes more intense, the increasing H atom extraction from CH_4 by H atoms is matched by a reforming step with H, resulting simply in a recombination of H atoms to form H_2. This effect becomes increasingly sensitive to hydrogen content with increasing hydrogren in the fuel mixture. Also for case D and E with less hydrogen, there is a shift so that the net of R31 and R32 shifts to becoming a small net destructor of CH_4. In the absence of H_2 consumption, hydrogen extraction by OH accounts for 85% of the consumption of CH_4. With increasing local hydrogen consumption the O atoms become slightly more influential, eventually leveling off at 25% of the methane consumption while OH comsumption decreases.

It is interesting to look at the carbon chemistry in more detail in the case in which there is significant hydrogen in the fuel. Figure 5 shows a typical snapshot of the methane destruction rate for Case B. In the figure we identify three subregions that correspond to the various generic features of this flame. Region A is burning intensely with positive curvature. Region B is a weakly burning with negative curvature. Region C has resulted from a large-scale flame-folding event, and will be discussed in more detail below.

Quantitative carbon path diagrams [24] represent the flow of carbon atoms through the various chemical species in the system as the fluid moves through the flame. Carbon path diagrams for these regions, normalized to the transfer rate of carbon atoms from CO to CO_2, are shown in Figure 6. Comparing the diagrams from regions A and B, we see significant shifts in the carbon and C_2 pathways. The carbon path through CH_3O increases from 4.2% to 7.7% (relative to the rate of C atoms through the $\mathrm{CO} \Leftrightarrow \mathrm{CO}_2$ path). The C_2 pathway shifts from 2.7% to 3.8%. So, moving from the intense cellular burning regions to the areas that are locally extinguished, the recombination-type reactions leading to C_2 molecules increases.

Region C in Figure 5 covers a gap in the flame where the consumption of H_2 is essentially zero. In this region however, we observe unusually high concentrations of C_2 hydrocarbons (see the insets, Fig. 5, b and c). In the path diagrams discussed above we observe shifts in carbon and C_2 paths for region C relative to those in region A, and these increases are somewhat larger than those seen in region B. Figure 7(a) shows the mean production rate of C_2H_4 as a function of T, over the entire computational domain, and over regions A, B and C. The corresponding quantity from the steady 1D (PREMIX) solution is included for reference. Interestingly, for all cases except region B, we see a reduction in the mean extreme values of this quantity at each interval in temperature relative to the PREMIX solution. We also see that the extremes in region C are smallest of all, even though the net production paths are larger. To shed further light on this situation, Figure 7(b) shows an image of the $\dot{\omega}_{C2H4}$ profile near region C, overlayed with contours in T. In the absence of local heat deposition by chemical reaction (in the cusp regions) the isotherms separate. The production (and destruction) of C_2 species such as C_2H_4 continues in these extinction zones, somewhat locked to the isotherms which are separating in physical space. The destruction is thereby delayed in time and the radicals are transported downstream. The isotherm separation thereby leads to extended local pockets of these flame radicals, even though they eventually are consumed. This process may also be interpreted as follows: some of the carbon "leaking" though the extinguished regions of the flame recombine to C_2 species rather than following the usual oxidation path to CO_2. However, the C_2 species eventually are destroyed in the post-flame region so that unburned hydrocarbons appear not to survive in the product stream.

4. Conclusion

We have investigated the combustion behavior of a range of methane-hydrogen fuel mixtures. The local flame speeds based on fuel consumption rate have strong correlations with the positive curvature for flames of the mixed fuels. The Markstein effects are stronger with higher H_2 content in the inlet fuel mixtures. When the fuel is 25% or more H_2 the flames show gaps within the flame surface characteristic of thermodiffusively unstable flames. Increasing H_2 fraction in the fuel mixtures also results in higher CH_4 consumption rate. Reaction pathways analysis of carbon chemistry show shifts in C and C_2 pathways from intensive burning to extinguished regions. For the high hydrogen cases, we see high concentration of C_2 species in the local extinction gaps but these species are slowly oxidized and no significant unburnt hydrocarbons exit the flame zone.

Acknowledgments

This work was supported by the DOE Applied Mathematics Research Program. Computations were performed on Lawrencium at LBNL and on Hopper at NERSC. All work was performed under U. S. Department of Energy Contract No. DE-AC02-05CH11231.

References

[1] D. Littlejohn, R. K. Cheng, *Proc. Comb. Inst.* 31 (2007) 3155–3162.

[2] R. K. Cheng, D. Littlejohn, P. A. Strakey, S. T., *Proc. Comb. Inst.* 32.

[3] D. Wicksall, A. Agrawal, R. Shefer, J. Kelley, *J. of Propulsion and Power* 21 (2005) 16–24.

[4] C. J. Lawn, R. W. Schefer, *Combust. Flame* 146 (1-2) (2006) 180–199.

[5] C. Cohé, F. Halter, C. C., I. Gökalp, L. $G\ddot{u}lder$, $\ddot{O}$. , *Proc. Combust. Inst.* 31 (2007) 1345–1352.

[6] F. Haller, C. Chauveau, I. Gökalp, *Int. J. Hydrogen Energy* 32 (2007) 2585–2592.

[7] C. Mandilas, M. P. Ormsby, G. G. W. Sheppard, R. Woolley, *Proc. Comb. Inst.* 31 (2007) 1443–1450.

[8] P. Strakey, T. Sidwell, J. Ontko, *Proc. Comb. Inst.* 31 (2) (2007) 3173–3180.

[9] H. S. Kim, A. V. K., G. A. K., *Int. J. Hydrogen Energy* 34 (2) (2009) 1063–1073.

[10] M. Fairweather, M. P. Ormsby, C. G. W. Sheppard, R. Woolley, *Combust. Flame* 156 (4) (2009) 780–790.

[11] G. S. Jackson, R. Sai, J. M. Plaia, C. M. Boggs, K. T. Kiger, *Combust. Flame* 132 (3) (2003) 503–511, erratum 135(3):363, 2003.

[12] E. Hawkes, J. H. Chen, *Combust. Flame* 138 (2004) 242–258.

[13] R. Sankaran, H. G. Im, *Combust. Sci. Tech.* 178 (9) (2006) 1585–1611.

[14] T. D. Dunstan, K. W. Jenkins, *Int. J. Hydrogen Energy* 34 (2009) 8389–8404.

[15] A. W. Vreman, J. A. van Oijen, L. P. H. de Goey, R. J. M. Bastiaans, *Int. J. of Hydrogen Energy* 34 (2009) 2778–2788.

[16] L. P. H. de Goey, R. T. E. Hermanns, R. J. M. Bastiaans, *Proc. Combust. Inst.* 31 (2007) 1031–1038.

[17] J. B. Bell, R. K. Cheng, M. S. Day, I. G. Shepherd, *Proc. Combust. Inst.* 31 (2007) 1309–1317.

[18] M. S. Day, J. B. Bell, P.-T. Bremer, V. Pascucci, V. Beckner, M. Lijewski, *Combust. Flame* 156 (2009) 1035–1045.

[19] M. S. Day, J. B. Bell, *Combust. Theory Modelling* 4 (2000) 535–556.

[20] A. Kazakov, M. Frenklach, *Reduced Reaction Sets based on GRI-Mech 1.2*, http://www.me.berkeley.edu/drm/, university of California at Berkeley.

[21] J. B. Bell, M. S. Day, J. F. Grcar, M. J. Lijewski, *Comm. App. Math. Comput. Sci.* 1 (1) (2005) 29–52.

[22] J. O. Hinze, *Turbulence*, 2nd Edition, McGraw-Hill, 1975.

[23] Y. Rastigejev, M. Matalon, *J. Fluid. Mech.* 554 (2006) 371–392.

[24] N. Sullivan, A. Jensen, P. Glarborg, M. S. Day, J. F. Grcar, J. B. Bell, C. Pope, R. J. Kee, *Combust. Flame* 131 (2002) 285–298.

Table 1: For the six mixtures investigated (A-F), the fuel is ϕ=0.7 methane-air, blended with f_H% of ϕ=0.37 hydrogen-air by volume, at T_{in}=298 K (f_H given in the table). The table also includes the laminar burning speed, s_{lam} (cm/s), temperature of peak fuel consumption, T_{peak} (K), and thermal thickness, $\delta_{lam} = (T_{ad} - T_{in})/\max(\nabla T)(mm)$, of a flat steady flame burning through the corresponding fuel (T_{ad} is the adiabatic flame temperature of the fuel).

Case	f_H	s_{lam}	T_{peak}	δ_{lam}
A	100	14.2	1144	0.800
B	87.5	11.1	1149	0.885
C	75	11.0	1212	0.899
D	50	12.4	1320	0.815
E	25	14.8	1407	0.696
F	0	18.4	1481	0.602

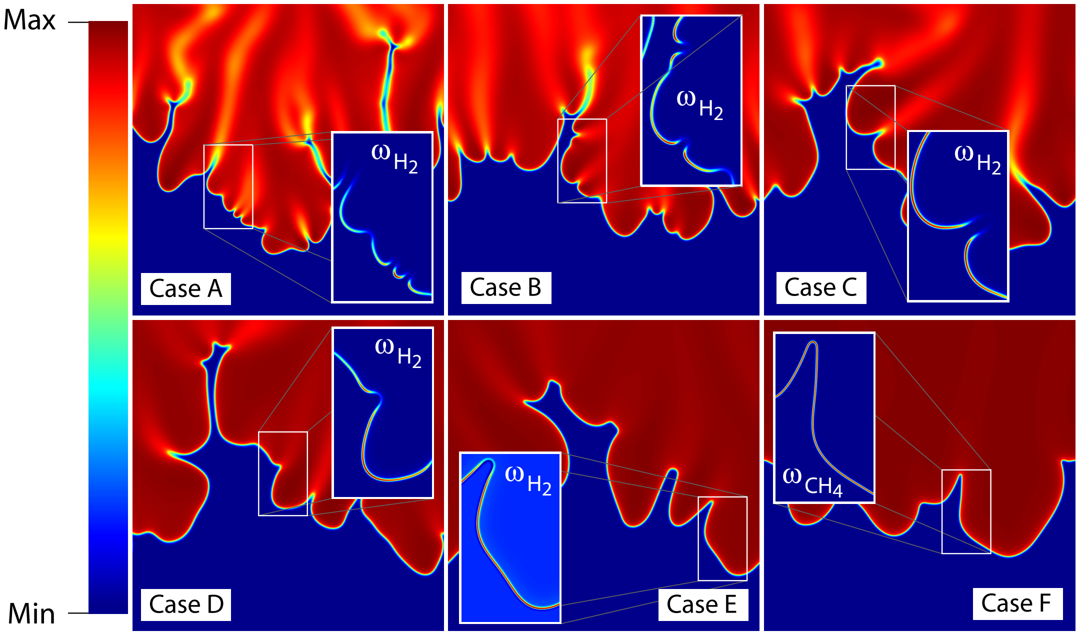

Figure 1: Images of typical flame segments showing H_2 (CH_4) fuel consumption rates for the six flames.

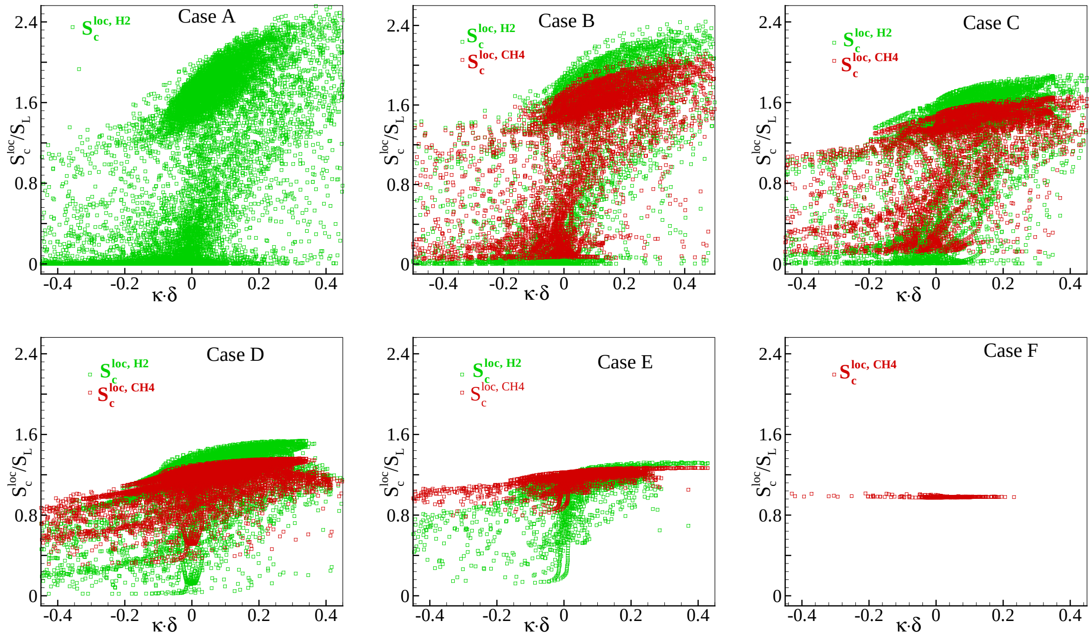

Figure 2: Comparisons of the local flame speeds based on both H_2 and CH_4 fuel consumption rates for the six flames.

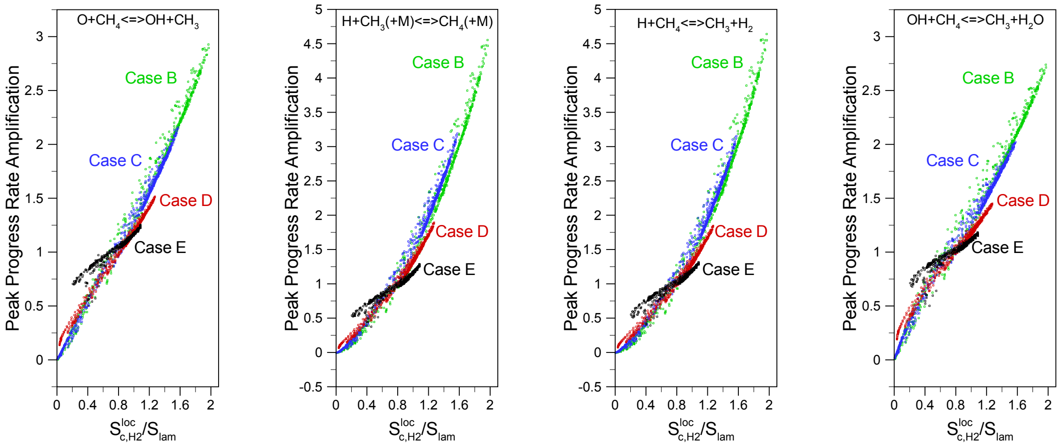

Figure 3: Peak rate of predominant CH_4 destruction routes in the quasi-steady 2D flame. Peak values here are taken from equi-spaced scans normal to flame, and are plotted against local H_2 burning speed. Peak reaction rates are normalized by the the peak rate values in the flat steady (Premix) flame.

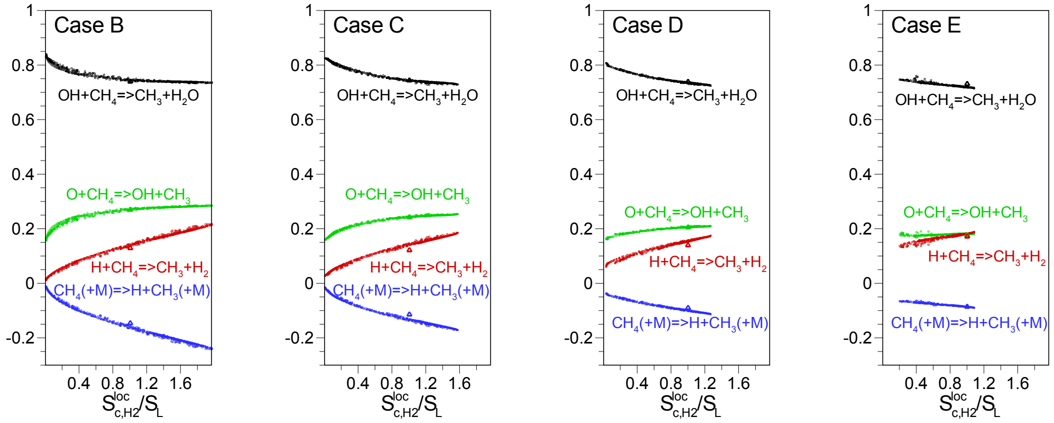

Figure 4: Predominant reactions involving CH_4 production/destruction: reaction rates are normalized by the local total destruction rate of CH_4.

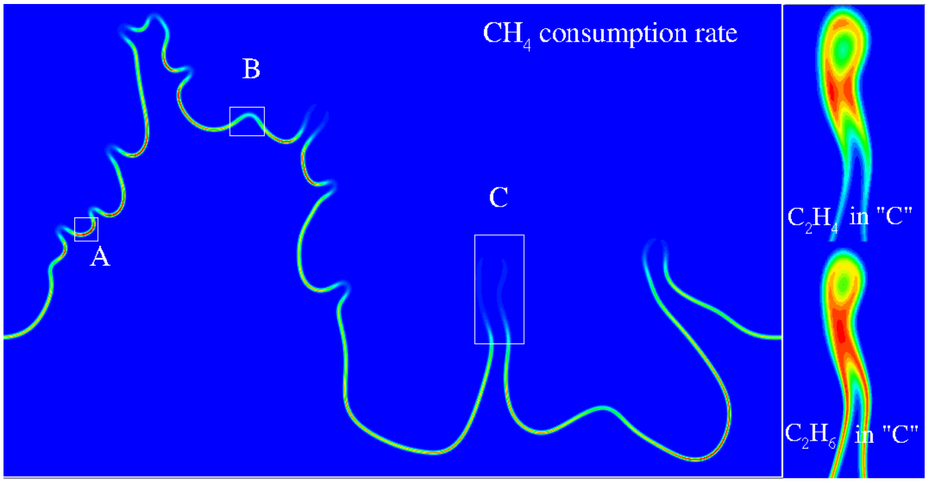

Figure 5: (a) Typical $\dot{\omega}_{\mathrm{CH4}}$ *from Case B, showing labelled subregions used for caborn path analysis. (b)* C_2H_4 *mole fraction in region C, (c)* C_2H_6 *mole fraction in region C.*

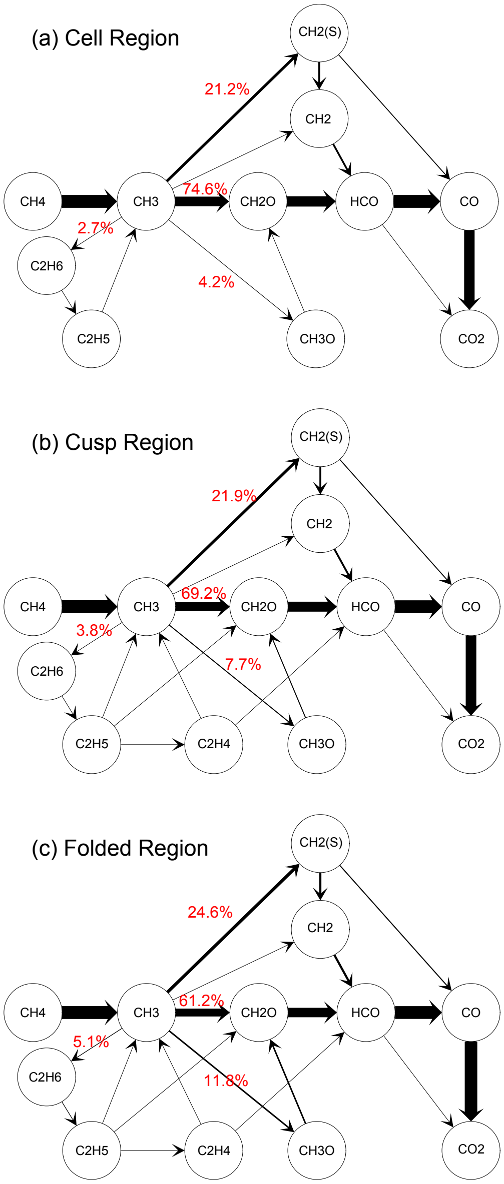

Figure 6: Carbon pathway diagrams of the three subregions indicated in Fig. 5.

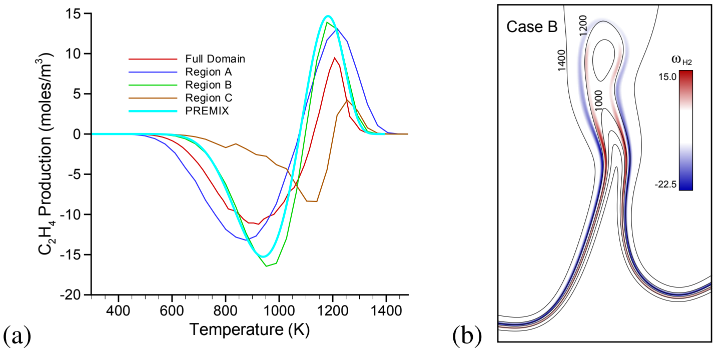

Figure 7: (a) Conditional mean production rate of C_2H_4 vs. T for Case B, taken over the entire domain, and also taken over the three regions shown in Fig. 5. The result from PREMIX is also shown for reference. (b) Production rate, $\dot{\omega}_{C2H4}$ (moles/m^3) near region C of Fig. 5, overlayed with contours in T.